Metal-insulator transition in V_2O_3 with intrinsic defects

Richard Tran, Xiang-Guo Li, and Shyue Ping Ong [*]

Department of NanoEngineering, University of California San Diego, 9500 Gilman Drive, Mail Code 0448,
La Jolla, California 92093-0448, USA

Yoav Kalcheim

Department of Materials Science and Engineering, Technion-Israel Institute of Technology, Haifa 32000, Israel

Ivan K. Schuller

Department of Physics and Center for Advanced Nanoscience, University of California San Diego, 9500 Gilman Drive,
Mail Code 0448, La Jolla, California 92093-0448, USA

Vanadium sesquioxide (V_2O_3) is a Mott insulator exhibiting a temperature-dependent metal-insulator transition (MIT) at 165 K accompanied by both a magnetic and structural transition. Although it is expected to be a metal under conventional band theory, electron interactions at low temperature cause it to behave like an insulator, making it difficult to accurately model its electronic properties with standard *ab initio* methods. As such, accurate theoretical assessments of the MIT with point defects requires special attention to the type of functionals used. In this study, we conclude that the PBE+U functional provides the best compromise between accuracy and efficiency in calculating the properties related to the MIT between low-temperature and high-temperature V_2O_3. We use this functional to explore the various influences that intrinsic point defects will have on the MIT in V_2O_3.

I. INTRODUCTION

Neuromorphic computers, which aim to mimic the computational functionality found in biological brains, have the potential to be far more efficient than traditional von Neumann architectures in a variety of tasks, including data processing and cognition. One potential implementation of a neuromorphic computer can be achieved using a sequence of neuristors that can process electric signals in response to time-dependent excitations. This signal must exceed a threshold and maintain its excited state for a period of time in a behavior referred to as "leaky, integrate, and fire" to emulate the short-term memory needed to sum inputs.

Quantum materials that undergo a metal-insulator transition (MIT) are ideal for such devices as they exhibit a sudden collapse of insulating behavior under an external stimuli, and they can gradually recover their insulating state over time in the absence of the stimuli. This behavior is known as volatile resistive switching. Vanadium oxides such as V_2O_3 and VO_2 are known to exhibit this functionality [1] and are considered model materials for studying such properties due to their chemical simplicity. Below a critical temperature (T_c) of 165 K, V_2O_3 is an antiferromagnetic insulator (AFI) with monoclinic space group $I2/a$ and a band gap (E_g) of 0.6 eV [2]. Above T_c, it is a paramagnetic metal (PM) adopting the corundum structure with trigonal space group $R\bar{3}c$.

Varying the temperature of a material to achieve a MIT can consume a lot of energy when scaled to an actual computing device. From an engineering standpoint, it is desirable to reduce this energy consumption as much as possible, either by decreasing the energy barrier (temperature) required to trigger the MIT or by avoiding a temperature-induced MIT altogether. Previous experiments [3,4] and density functional theory (DFT) calculations [5] have shown that V_2O_3 may be more suitable for such applications than VO_2 due to its lower energy barrier for MIT, resulting in a faster switching speed. Further, introducing defects is a pathway to modulate the MIT behavior of V_2O_3.

While many defect studies in V_2O_3 have been focused on transition-metal doping, most notably for Cr and Ti doping [5–7], intrinsic defects have garnered less attention. One such study was done by Ramirez *et al.* [8], who demonstrated that while the resistance change is more or less stable, the transition temperature does go down substantially with the dose of defect-induced ion bombardment. However, they observed a sudden and complete breakdown in MIT and structural phase transition (SPT) at a concentration of 2×10^{14} ions. Wickramaratne *et al.* [9] used DFT to study Frenkel defects in V_2O_3 to explain the origins of these effects. They demonstrated that the V-Frenkel defect reduced the spin-flip energy by a factor of 3, thus reducing the energy barrier for the Slater AFI to PM transition. Ueda *et al.* [10] explored the effect of nonstoichiometry in V_2O_{3+x} and compared it to Ti-doped V_2O_3 and pressurized V_2O_3. They showed that nonstoichiometry reduces the transition temperature of the AFI phase as x

*ongsp@eng.ucsd.edu

increases up to 0.03, beyond which the AFI phase breaks down to an antiferromagnetic metallic phase. Similarly, Bao *et al.* [11] used neutron diffraction to find this phase for $V_{2-y}O_3$ with a Néel temperature (T_N) of 9 K. More recently it has been experimentally shown that V_2O_3 exhibits nonthermal switching when defects are introduced [12]. This is achieved via the Poole-Frenkel effect whereby trapped carriers occupying in-gap states can hop into the conduction band whose energy barrier has been reduced by an external potential.

DFT methods have been used to study the MIT in vanadium oxides. Due to their Mott-insulating nature [13–15], a Hubbard U correction, typically fitted to reproduce the experimental band gaps, needs to be applied for semilocal functionals such as the Perdew-Berke-Ernzerhof (PBE) generalized gradient approximation (GGA) [16] to account for the repulsion arising from electron correlation. Alternatively, hybrid functionals that include a fraction of exact exchange have also been found to successfully predict an insulating state for low-temperature (LT) V_2O_3 and VO_2 [17,18]. However, the Heyd-Scuseria-Ernzerhof (HSE) functional in particular has also been shown to incorrectly predict an insulating high-temperature (HT) and magnetically ordered LT phase for VO_2 [19]. Stahl and Bredow [20] had recent success using the meta-GGA strongly constrained and appropriately normed (SCAN) functional to simultaneously predict four key properties—a band gap in the LT nonmagnetic phase, a metallic state for the HT phase, and the correct energy difference between the HT and LT phases in VO_2.

In this work, we perform a comprehensive evaluation of different DFT functionals—PBE and SCAN, with and without Hubbard U, as well as HSE—in reproducing the key energetic and electronic structure properties of LT and HT V_2O_3. This will be followed by an in-depth investigation of defects in the LT and HT phases of V_2O_3 and how they introduce carrier traps and influence the band gap of the LT phase, which can yield potential insights into the origins of nonthermal MIT in V_2O_3.

II. METHODS

A. DFT calculations

All DFT [22] calculations were performed using the Vienna Ab initio Simulation Package (VASP) [21] within the projector augmented wave (PAW) [23] approach. The plane-wave cutoff energy was 400 eV [17], and the energies and atomic forces were converged to within 10^{-4} eV and 0.02 eVÅ^{-1}, respectively. Gaussian and Methfessel-Paxton [24] smearing were used for the insulating LT and metallic HT phases, respectively. Γ-centered k-point densities per unit reciprocal length of 30 and 85 Å^{-1} were used for the relaxation of supercells and for density of states (DOS) calculations, respectively. The exchange-correlation functionals tested in this work are PBE, PBE+U, SCAN, SCAN+U, and HSE. The U parameter was set at 2.68 and 1.35 eV for PBE+U and SCAN+U, respectively, which were found to reproduce the experimental band gap of LT V_2O_3, i.e., 0.6 eV [see Fig. S1(a) in the Supplemental Material [25]] [2,26,27].

All analysis and input generation was performed with the Python Materials Genomics (pymatgen) library [28].

B. Initial structures and magnetic configurations

As with previous experimental and computational works [29,30], we found that the most stable antiferromagnetic configuration of LT V_2O_3 has V atoms ferromagnetically aligned on the (010) planes with each consecutive plane being oppositely aligned along the [010] direction, as shown in Fig. 1(a).

The HT phase is known to be paramagnetic. In this work, we investigated both ferromagnetic and nonmagnetic initializations as it was found that an antiferromagnetic initialization causes the HT corundum phase to automatically relax to the LT monoclinic phase.

C. Intrinsic defects

In this work, we focus on vacancies and interstitials. Using the Kröger-Vink notation, vacancies and interstitials are indicated by v_A and A_i, respectively, where A is the species of the defect. Note that a lower case v is used to denote vacancies to distinguish from the symbol for vanadium. Negative and positive charges are indicated by ′ and • superscripts, respectively. V and O interstitial sites were found using the Interstitialcy Finding Tool (InFiT) [31]. The algorithm found four symmetrically distinct interstitial sites in the LT phase and one symmetrically distinct site in the HT phase.

We investigated both charged and neutral defects using the method described by Broberg *et al.* [32]. A nominal oxidation state of -2 was assumed for the oxygen anion, and charges ranging from 0 to -2 (0 to $+2$) for O_i (v_O) were introduced by adding (subtracting) an integer number of electrons. The same method, *mutatis mutandis*, was applied for charged defects involving V_i and v_V assuming an oxidation state of $+3$ for the vanadium cation. Charged defects were investigated only for the insulating LT phase.

All defect calculations were performed using $2\times2\times2$ (160 atoms) and $2\times2\times1$ (120 atoms) supercells of the conventional unit cells for the LT and HT phases, respectively. We have confirmed that this supercell size is sufficient to minimize any interactions between periodic boundary images and their consequent effect on E_g and the band edges [see Fig. S2].

D. Thermodynamic analysis

The defect formation energy is calculated with the following equation:

$$E_{\text{form}}[X^q] = E_{\text{tot}}[X^q] - E_{\text{tot}}[\text{bulk}]$$
$$- \sum n_i[E_i + \Delta\mu_i(T, P_0)] + q\varepsilon_F + E_{\text{corr}}^q, \quad (1)$$

where $E_{\text{tot}}[X^q]$ and $E_{\text{tot}}[\text{bulk}]$ are the total DFT energies of the supercell with and without the defect X, respectively. n_i is the number of species i added ($n_i > 0$) or removed ($n_i < 0$) from the supercell. $\Delta\mu_i(T, P)$ is the chemical potential for species i relative to the energy per atom of species i. The chemical potentials of Eq. (1) can be rewritten in terms of $\Delta\mu_O$ only by substituting μ_V for Eq. (S1). As such, all calculations of E_{form} will be done with respect to $\Delta\mu_O$ as a function of temperature T and partial pressure P_0. It should be noted that an anion correction ($E_{\text{corr}}^O = -0.702$ eV) is applied to $\Delta\mu_O$ to compensate for the overbinding of O_2 under PBE and PBE+U
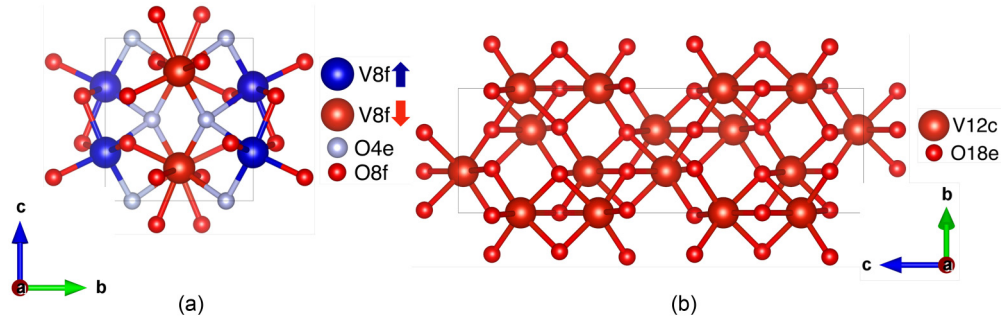
FIG. 1. Conventional unit cells of (a) the LT monoclinic ($I2/a$) and (b) the HT corundum ($R\bar{3}c$) phases of V$_2$O$_3$. The Wyckoff symbols and spin directions (large red/blue spheres correspond to opposite spins) of each symmetrically distinct site are given on the right of each structure.

[33]. As such, the relative chemical potential of oxygen is in reference to the DFT calculated energy of O$_2$ per atom and the following correction:

$$\Delta\mu_O(T, P_0) = \mu_O - \frac{1}{2}E_{O_2} - E_{corr}^O \tag{2}$$

with the allowed range of $\Delta\mu_O(T, P_0)$ being

$$-4.35 \text{ eV} = \Delta G_{V_2O_3} < \Delta\mu_O(T, P_0) < 0 \text{ eV}, \tag{3}$$

where $\Delta G_{V_2O_3}$ is the formation energy of V$_2$O$_3$ [see the Supplemental Material [25] for more details with regard to the chemical potential].

For charged defects, the fourth term, $q\varepsilon_F$, compensates for the charge where ε_F is the Fermi level and ranges between the valence-band maximum (VBM) and the conductance-band minimum (CBM) in the DOS [see Fig. 4(a)]. E_{corr}^q is the Freysoldt correction term for charged defects in a supercell [34]. See the Supplemental Material [25] for a more detailed discussion of these quantities.

From E_{form}, the thermodynamic transition level between charged states q_1 and q_2, which determines the Fermi level of carrier traps, is given as follows:

$$\varepsilon_F(q_1, q_2) = \frac{E_{form}[X^{q_1}] - E_{form}[X^{q_2}]}{q_2 - q_1}. \tag{4}$$

The MIT temperature T_c in the presence of a defect can be calculated with the following equation [35]:

$$T_c = T_{c,0}\frac{\Delta H}{\Delta H_0}, \tag{5}$$

where $T_{c,0} = 165$ K is the experimental MIT temperature of stoichiometric V$_2$O$_3$, and ΔH_0 and ΔH are the changes in enthalpy during LT and HT phase transition for stoichiometric and nonstoichiometric V$_2$O$_3$, respectively. Here, the enthalpy (H) is approximated using the total relaxed DFT energy on the assumption that the pV and TS terms are negligible.

III. RESULTS

A. Functional assessment of bulk properties

Figure 2 summarizes the ability of five functionals—PBE, PBE+U, SCAN, SCAN+U, and HSE—to reproduce the correct band gap (a) and relative energetics (b) of LT and HT V$_2$O$_3$. All functionals predict the HT phase to be metallic ($E_g^{HT} = 0$ eV). However, the PBE functional incorrectly predicts the LT phase to be metallic, while the SCAN and HSE

functionals lead to a severe underestimation and overestimation of the band gap E_g^{LT}, respectively. For the PBE+U and SCAN+U functionals, the Hubbard U parameters were calibrated to reproduce the experimental band gap of LT V$_2$O$_3$, i.e., 0.6 eV exactly [see Fig. S1(a) in the Supplemental Material [25]].

Table I provides an overview of the qualitative functional performance in predicting the properties of LT and HT V$_2$O$_3$. All functionals predict the LT phase to have an antiferromagnetic ground state [see Table S1 in the Supplemental Material [25]]. While all functionals also predict the AFI LT phase to be more stable than the ferromagnetic metallic (FM) HT phase, there are substantial differences in the energy difference of up to 100 meV/f.u. between the HT and LT phase ($\Delta E_{V_2O_3}^{HT\text{-}LT}$). It is known experimentally that the energy difference between HT and LT VO$_2$, $\Delta E_{VO_2}^{HT\text{-}LT}$, is approximately 44 meV/f.u. [36]. Since $T_c^{VO_2} > T_c^{V_2O_3}$ ($T_c^{VO_2} = 340$ K), $\Delta E_{V_2O_3}^{HT\text{-}LT} < \Delta E_{VO_2}^{HT\text{-}LT} \sim 44$ meV/f.u. The PBE, PBE+U, and HSE functionals produce values of $\Delta E_{V_2O_3}^{HT\text{-}LT}$ that satisfy this additional constraint as
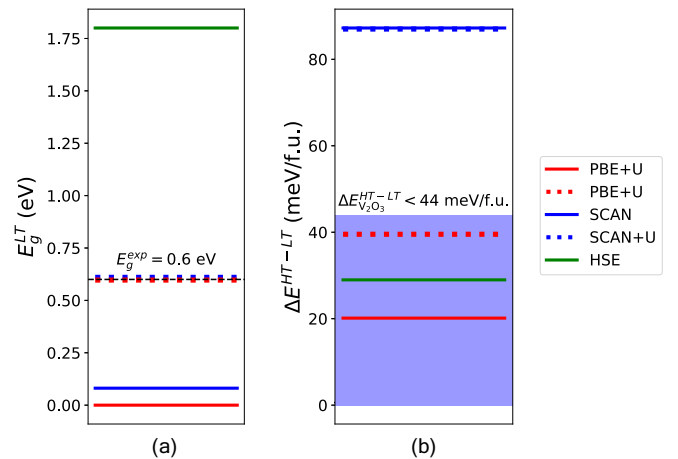

FIG. 2. Plots of the band gap of (a) the LT AFI phase of V$_2$O$_3$ and (b) the energy difference per formula unit relative to the HT FM phase for the PBE, PBE+U, SCAN, SCAN+U, and HSE functionals. The U parameters of 2.68 and 1.35 eV for PBE+U and SCAN+U, respectively, were calibrated to reproduce the experimental band gap of LT V$_2$O$_3$. The dashed black line indicates the experimental band gap, and the blue shaded region indicates the expected energy difference for V$_2$O$_3$.

TABLE I. An overview of the ability of the five functionals in reproducing the four key qualitative properties of V_2O_3: (i) The LT phase is more stable than the HT phase ($E^{LT} < E^{HT}$); (ii) the LT phase is insulating (i.e., $E_g^{LT} > 0$ eV); (iii) the HT phase is metallic (i.e., $E_g^{HT} = 0$ eV); (iv) the LT phase is antiferromagnetic (AFM). * indicates a caveat in fulfilling a criterion.

	$E^{LT} < E^{HT}$	$E_g^{LT} > 0$	$E_g^{HT} = 0$	LT is AFM
PBE	✓	×	✓	✓
PBE+U	✓	✓	✓	✓
SCAN	✓*	✓*	✓	✓
SCAN+U	✓*	✓	✓	✓
HSE	✓	✓*	✓	✓

shown in the blue shaded region. The SCAN and SCAN+U functionals overestimate $\Delta E_{V_2O_3}^{HT\text{-}LT}$ by a significant margin.

We also investigated the accuracy of each functional in reproducing the experimental lattice parameters of the LT and HT phases [37,38], as shown in Table S2 in the Supplemental Material [25]. For the monoclinic LT phase, the calculated lattice lengths are within 0.07 Å of the experimental values for the PBE+U, SCAN, SCAN+U, and HSE functionals. The PBE functional, however, leads to errors of >0.1 Å for the a and b lattice parameters and 2° for β. For the HT phase in the hexagonal setting, the PBE+U functional has the largest deviation from the experimental lattice parameters with an overestimation of 0.17 and 0.1 Å for a and c, respectively. In both phases, the SCAN functional yielded lattice parameters that are closest to the experimental values with errors of <0.03 Å for the lattice lengths. The space group of both phases is preserved in all cases after structural relaxation.

Based on the above results, we have elected to use the PBE+U functional with $U_{eff} = 2.68$ eV to study the MIT in stoichiometric and nonstoichiometric V_2O_3. This functional choice yields values of $\Delta E^{HT\text{-}LT}$ and E_g^{LT} consistent with experimental observations, albeit at the expense of somewhat larger errors in the lattice parameters. The subsequent results in this work are based on this functional choice.

B. Charged defects in LT AFI V_2O_3

The calculated defect phase diagram in LT AFI V_2O_3 as a function of oxygen chemical potential $\Delta\mu_O$ (temperature) and Fermi energy ε_F is given in Fig. 3. Under less reducing conditions, vanadium vacancies v_V are the most stable defects (red regions). At the most oxidizing conditions of $\Delta\mu_O > -2.1$ eV ($T < 1754$ K at standard atmospheric conditions), vanadium-deficient V_2O_3 is predicted to be stable relative to stoichiometric V_2O_3 ($E_{form} < 0$ eV). As conditions become more reducing (blue regions), oxygen vacancies v_O on the $4e$ site become the most stable defects. Previous annealing experiments performed under ultrahigh-vacuum by Simic-Milosevic *et al.* [27] found the formation of v_O in bulk V_2O_3 between 600 and 700 K. While our computed temperatures for the formation of v_O are far above these temperatures, it should be noted that these temperatures are only estimates that neglect any entropic contributions from solid phases. Nevertheless, our results are in qualitative agreement with experiments where v_O is predicted to form well above T_c.
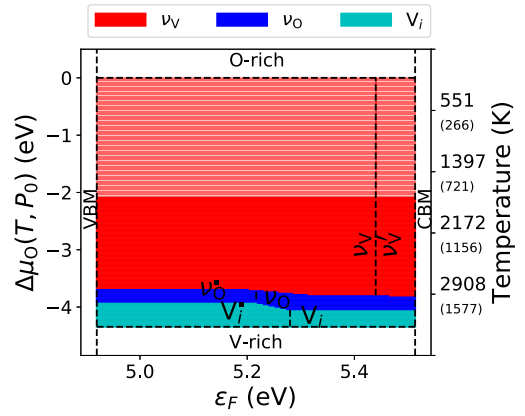

FIG. 3. Stability map for charged and neutral defects in LT V_2O_3 as a function of ε_F and $\Delta\mu_O$. The legend at the top indicates the colors representing defect types. The lighter red region indicates where the formation of vanadium-deficient V_2O_3 is favorable relative to stoichiometric V_2O_3, i.e., $E_{form} < 0$ eV, while the solid red region indicates $E_{form} > 0$ eV. Vertical dashed lines indicates a transition between charged states in a defect. Two corresponding temperature scales derived from the JANAF thermochemical tables [39] are provided as the secondary y axis on the right [see the Supplemental Material [25]]. The temperature scales are based on two partial pressures of oxygen: $p_0 = 0.1$ MPa, i.e., standard atmospheric conditions, and $p_0 = 10^{-13}$ MPa, i.e., ultrahigh-vacuum conditions (parentheses).

Finally, under the most reducing conditions (cyan regions), vanadium interstitials V_i are the most stable. Given the lack of any previous experimental evidence of vanadium interstitial formation, the remainder of this work will be primarily focused on vacancy defects.

The transition between different defect charge states can be determined using Eq. (4). For example, the neutral vanadium vacancy v_V is predicted to be stable at ε_F of 5.44 eV, but the negatively charged v_V' is predicted to be stable above 5.44 eV. Similarly, the oxygen vacancy transitions from $v_O^\bullet$ to v_O at $\varepsilon_F \approx \frac{\text{VBM+CBM}}{2}$.

Figure 4 shows the DOS of LT AFI V_2O_3 with vacancies with the stoichiometric DOS as a reference [Fig. 4(a)] along with the charge transition levels of v_V and v_O. All vacancy defects lead to a decrease in the band gap relative to stoichiometric V_2O_3. The v_V defect lowers the CBM and VBM by 0.23 and 0.11 eV, respectively, leading to a decrease in E_g from 0.59 to 0.53 eV as shown in Fig. 4(b). In Fig. 4(c), v_V' introduces additional spin-polarized states that slightly raise the VBM level while lowering the CBM by 0.12 eV, leading to a significant reduction in E_g to 0.45 eV. As ε_F increases, the charge carrier is trapped at a localized in-gap state as it transitions from v_V to v_V'. The activation energy for the conductivity of the trapped carrier (E_a) is about 73 meV relative to the CBM of stoichiometric V_2O_3. The transition state exists above the lowered CBM of vanadium vacancies allowing the trapped carrier to immediately conduct.

In Fig. 4(d), the CBM and VBM remain relatively unchanged when $v_O^\bullet$ is introduced, leaving E_g for the most part unchanged (0.56 eV). The most significant decrease in E_g comes from the introduction of v_O as shown in Fig. 4(e),
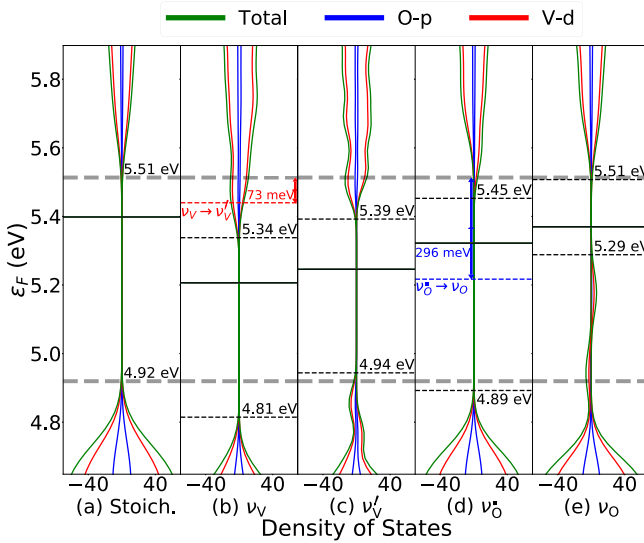
FIG. 4. Total (green), O-$2p$ (blue), and V-$3d$ (red) orbital DOS for a $2\times2\times2$ supercell of (a) LT stoichiometric V₂O₃ and nonstoichiometric V₂O₃ containing a (b) v_V, (c) v'_V, (d) $v^{\bullet}_O$, or (e) v_O defect. The VBM and CBM of the nonstoichiometric V₂O₃ (black dashed lines) as well as the Fermi level (black solid line) are also provided for each DOS. The stoichiometric VBM and CBM (gray dashed lines) are also provided for reference. The corresponding activation energies for carrier conductivity (E_a), i.e., the energy difference between the stoichiometric CBM and transition levels (dashed lines), are also annotated in (b) (red) and (d) (blue).

where additional spin-polarized states raise the VBM level by 0.37 eV to significantly reduce E_g to 0.22 eV. The transition of the oxygen vacancy from $v^{\bullet}_O$ to v_O occurs in the middle of the band gap with $E_a = 296$ meV relative to the CBM of stoichiometric V₂O₃. However, the transition to v_O results in the charge carrier falling below the valence band of v_O.

We performed Bader charge analysis to assess the effect of vacancies on the charges of atoms surrounding the defects

[40]. Figure 5 shows the change in Bader charge in the V₂O₃ supercell containing v_V and v_O. Using the Bader charges of stoichiometric V₂O₃ as a reference, we find that the charge on the oxygen nearest neighbors of v_V [Fig. 5(a)] becomes less negative from -1.24 to -1.12. We also observe a positive charge increase from $+1.87$ to $+2.07$ on three neighboring vanadium atoms within 3.4 Å from the vacancy. This is consistent with previous observations that LT V₂O₃ is a p-type semiconductor as a consequence of vanadium vacancies [27,41].

In contrast, the charge on the nearest-neighbor vanadium of v_O becomes less positive from $+1.87$ to $+1.67$. Furthermore, the electron carriers are confined to these nearest neighbors while the hole carriers of vanadium vacancies are present in the nearest neighbors as well as three additional surrounding vanadium atoms within 3.4 Å from the vacancy. This suggests that holes are more delocalized than electrons making hole carriers more conductive, which explains the lower E_a for v_V.

C. Effect of defects on MIT

Figure 6 plots the formation energy for neutral defects E_{form} as a function of $\Delta\mu_O$ in the LT monoclinic AFI and HT corundum FM phases of V₂O₃. As the stoichiometric FM HT V₂O₃ is 2.08 eV/f.u. lower in energy than the NM HT V₂O₃, we will focus on the AFI LT and FM HT phases here. The corresponding plots for the NM phase are presented in Fig. S2 in the Supplemental Material [25], and the relative stability of defects is the same in both the FM and NM configurations. As with the LT phase, the vanadium vacancy is more stable than the other defects in the HT phase. The formation energy of v_V in the HT FM phase is lower (more stable) than that of the LT phase by 0.26 eV. As such, the stabilization of v_V over stoichiometric V₂O₃ also occurs when $\Delta\mu_O > -2.255$ eV. v_O becomes the most stable defect at $\Delta\mu = -3.87$ eV in the HT phase, but never more stable than stoichiometric HT V₂O₃.

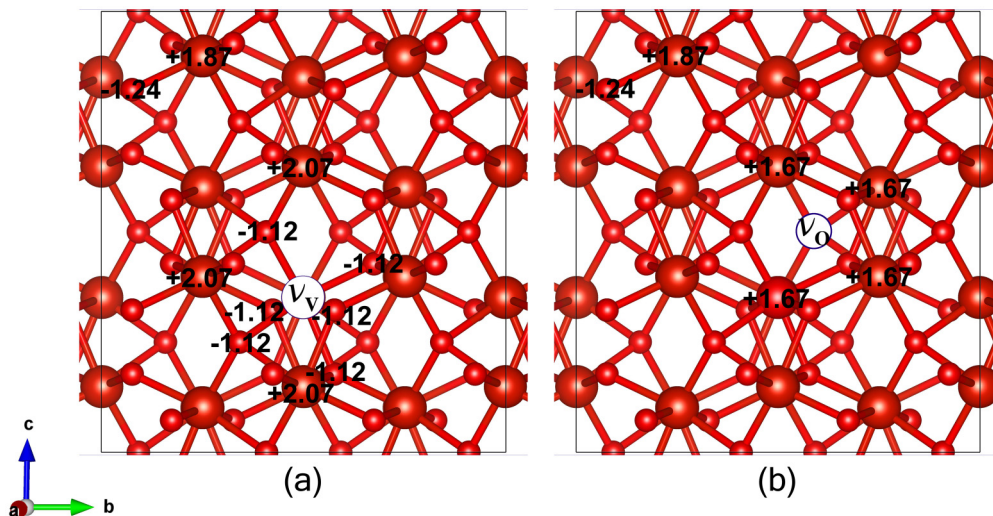Table II shows the calculated transition temperature T_c between the LT AFI phase and the HT FM phase for

FIG. 5. The $2\times2\times2$ supercell of V₂O₃ containing v_V (a) and v_O (b). All sites with Bader charges that differ from bulk-like charges are labeled, while all other sites have bulk-like charges. Bulk-like charges are labeled on the top left sites for oxygen (-1.24) and vanadium ($+1.87$).

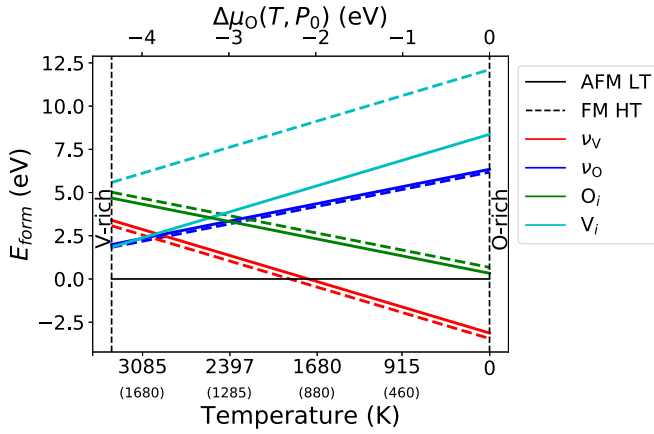FIG. 6. The neutral defect formation energy (E_{form}) for O_i, V_i, v_V, and v_O in LT AFI (solid) and HT FM (dashed) V_2O_3 as a function of the oxygen chemical potential ($\Delta\mu_O$, top x axis). The temperature scales based on $p_0 = 0.1$ ($p_0 = 10^{-13}$ MPa in parentheses) is provided on the bottom x axis.

stoichiometric and nonstoichiometric V_2O_3 using Eq. (5). Oxygen vacancies increase the LT AFI $\rightarrow$ HT FM T_c from 165 to 168 K (1.6% change). In contrast, a vanadium vacancy will significantly decrease T_c from 165 to 119 K (-27.9%).

IV. DISCUSSION

Here, we will provide a discussion of our computed results in the context of previous experiments on the application of V_2O_3 MIT for neuromorphic computing. Using the PBE+U functional, we have clearly demonstrated that v_V are the most stable defects under a reasonable device operation temperatures, which is consistent with past experiments [10,27]. Further, we have shown that v_V decreased T_c of MIT for V_2O_3 by 28% when transitioning from the AFI to the FM phase at a stoichiometric ratio of $V_{1.98}O_3$ (one vanadium vacancy in a 160-atom system), which is very close to the T_c decrease of 23.4% observed by Ueda et al. [10] for $V_{1.99}O_3$.

One proposed mechanism for the nonthermal MIT observed by Kalcheim et al. [12] is the Poole-Frenkel effect whereby the electric field reduces the energy barrier for excitation of trapped carriers from in-gap states into the conduction band [42]. Our calculations provide support for this mechanism. As shown in Fig. 4, vanadium vacancies result in the formation of trapped charge carriers around $E_a = 73$ meV below the CBM of V_2O_3. An applied field can decrease this barrier for carriers to hop into the energetically lowered conduction band of V_2O_3 thereby allowing for a purely

electric-field-induced MIT. Our calculated activation energy for carrier conductivity under vanadium vacancies is similar to that observed by Kalcheim et al. [12] ($E_a = 60$ meV). Future spectroscopic measurements will be needed to confirm the existence of these carrier traps to further support this hypothesis. The results also suggest that other doped materials with trapped charge carriers at a similar level below the CBM may exhibit electric-field-induced MIT; this is another hypothesis that would benefit from further experimental validation.

The calculated formation energies predict that the FM HT phase is more stable than the AFI phase in the presence of v_V. This is consistent with the results of Ramirez et al. [8], who demonstrate a sudden breakdown of MIT in V_2O_3 at an ion bombardment concentration above 2×10^{14} ions/cm^2. This was accompanied by a breakdown in structural phase transition (SPT) whereby the corundum phase is stable even below the stoichiometric critical temperature of 165 K. The ions were not found to be embedded in the actual V_2O_3 sample, which is an indicator of intrinsic defects being introduced. In contrast, VO_2 exhibits no SPT or MIT breakdown despite having a higher concentration of ion bombardment. Past computational results of VO_2 [43] showed O_i and v_O to be the dominant defects in VO_2, with LT VO_2 being able to easily recover its stoichiometric state via the diffusion of oxygen from the air [44]. However, such a recovery would not be possible with the vanadium defects in V_2O_3, which could explain the breakdown of SPT and MIT in V_2O_3 but not VO_2.

V. CONCLUSION

To conclude, we explored the performance of five DFT functionals in assessing the bulk properties of HT and LT V_2O_3 with regard to Mott insulation, and we concluded that the PBE+U functional provides the best compromise in computational accuracy and efficiency. It was shown that vanadium vacancies are the most stable defects under typical device operation temperatures. Vanadium vacancies can influence MIT in two ways. They can decrease the critical temperature required to induce the transition from the monoclinic low-temperature AFI phase and the corundum high-temperature FM phase. They can also lead to a nonthermal transition whereby a hole carrier hops from an in-gap state to the CBM whose energetic barrier is decreased due to an external potential (the Poole-Frenkel effect). These mechanisms can help reduce the energy consumption of neuromorphic devices. We will apply this analysis to other vanadate materials for a more comparative study in the future.

TABLE II. Phase transition critical temperature T_c of stoichiometric and nonstoichiometric V_2O_3. Percentage change in T_c relative to that of stoichiometric V_2O_3 is indicated in the last column.

LT $\rightarrow$ HT transition	Defect	T_c (K)	Percentage change
AFI $\rightarrow$ PM		165	
AFI $\rightarrow$ FM	v_V	119	-27.9%
AFI $\rightarrow$ FM	v_O	168	1.6%

[1] J. del Valle, J. G. Ramírez, M. J. Rozenberg, and I. K. Schuller, J. Appl. Phys. **124**, 211101 (2018).

[2] G. A. Thomas, D. H. Rapkine, S. A. Carter, A. J. Millis, T. F. Rosenbaum, P. Metcalf, and J. M. Honig, Phys. Rev. Lett. **73**, 1529 (1994).

[3] A. Zimmers, L. Aigouy, M. Mortier, A. Sharoni, S. Wang, K. G. West, J. G. Ramirez, and I. K. Schuller, Phys. Rev. Lett. **110**, 056601 (2013).

[4] T. Hennen, D. Bedau, J. A. Rupp, C. Funck, S. Menzel, M. Grobis, R. Waser, and D. J. Wouters, in *Proceedings of the 2019 IEEE 11th International Memory Workshop, IMW 2019* (IEEE, Piscataway, NJ, 2019), pp. 1–4.

[5] Y. Guo and J. Robertson, Microelectron. Eng. **109**, 278 (2013).

[6] D. B. McWhan, T. M. Rice, and J. P. Remeika, Phys. Rev. Lett. **23**, 1384 (1969).

[7] D. B. McWhan, A. Menth, J. P. Remeika, W. F. Brinkman, and T. M. Rice, Phys. Rev. B **7**, 1920 (1973).

[8] J. G. Ramirez, T. Saerbeck, S. Wang, J. Trastoy, M. Malnou, J. Lesueur, J.-p. Crocombette, J. E. Villegas, and I. K. Schuller, Phys. Rev. B **91**, 205123 (2015).

[9] D. Wickramaratne, N. Bernstein, and I. I. Mazin, Phys. Rev. B **99**, 214103 (2019).

[10] Y. Ueda, K. Kosuge, and S. Kachi, J. Solid State Chem. **31**, 171 (1980).

[11] W. Bao, C. Broholm, S. A. Carter, T. F. Rosenbaum, G. Aeppli, S. F. Trevino, P. Metcalf, J. M. Honig, and J. Spalek, Phys. Rev. Lett. **71**, 766 (1993).

[12] Y. Kalcheim, A. Camjayi, J. del Valle, P. Salev, M. Rozenberg, and I. K. Schuller, Nat. Commun. **11**, 2985 (2020).

[13] Z. Zhu and U. Schwingenschlögl, Phys. Rev. B **86**, 075149 (2012).

[14] A. J. Cohen, P. Mori-Sánchez, and W. Yang, Science **321**, 792 (2008).

[15] Y. Zhou and S. Ramanathan, Proc. IEEE **103**, 1289 (2015).

[16] J. P. Perdew, K. Burke, and M. Ernzerhof, Phys. Rev. Lett. **77**, 3865 (1996).

[17] N. J. Szymanski, Z. T. Y. Liu, T. Alderson, N. J. Podraza, P. Sarin, and S. V. Khare, Comput. Mater. Sci. **146**, 310 (2018).

[18] Y. Guo, S. J. Clark, and J. Robertson, J. Chem. Phys. **140**, 054702 (2014).

[19] R. Grau-Crespo, H. Wang, and U. Schwingenschlögl, Phys. Rev. B **86**, 081101(R) (2012).

[20] B. Stahl and T. Bredow, J. Comput. Chem. **41**, 1 (2019).

[21] G. Kresse and J. Furthmüller, Phys. Rev. B **54**, 11169 (1996).

[22] W. Kohn and L. J. Sham, Phys. Rev. **140**, A1133 (1965).

[23] J. Lehtomäki, I. Makkonen, M. A. Caro, A. Harju, and O. Lopez-Acevedo, J. Chem. Phys. **141**, 234102 (2014).

[24] M. Methfessel and A. T. Paxton, Phys. Rev. B **40**, 3616 (1989).

[25] See Supplemental Material at http://link.aps.org/supplemental/10.1103/PhysRevB.103.075134 for further details of the functional analysis, derivation of $\Delta \mu_O$, and the density of states and defect formation energy of HT FM and NM V$_2$O$_3$.

[26] L. F. Mattheiss, J. Phys.: Condens. Matter **6**, 6477 (1994).

[27] V. Simic-Milosevic, N. Nilius, H.-P. Rust, and H.-J. Freund, Phys. Rev. B **77**, 125112 (2008).

[28] S. P. Ong, W. D. Richards, A. Jain, G. Hautier, M. Kocher, S. Cholia, D. Gunter, V. L. Chevrier, K. A. Persson, and G. Ceder, Comput. Mater. Sci. **68**, 314 (2013).

[29] R. M. Moon, Phys. Rev. Lett. **25**, 527 (1970).

[30] D. Grieger and M. Fabrizio, Phys. Rev. B **92**, 075121 (2015).

[31] N. E. Zimmermann, M. K. Horton, A. Jain, and M. Haranczyk, Front. Mater. **4**, 1 (2017).

[32] D. Broberg, B. Medasani, N. E. Zimmermann, G. Yu, A. Canning, M. Haranczyk, M. Asta, and G. Hautier, Comput. Phys. Commun. **226**, 165 (2018).

[33] S. P. Ong, S. Cholia, A. Jain, M. Brafman, D. Gunter, G. Ceder, and K. A. Persson, Comput. Mater. Sci. **97**, 209 (2015).

[34] C. Freysoldt, J. Neugebauer, and C. G. Van de Walle, Phys. Rev. Lett. **102**, 016402 (2009).

[35] M. Netsianda, P. E. Ngoepe, C. R. A. Catlow, and S. M. Woodley, Chem. Mater. **20**, 1764 (2008).

[36] F. Pintchovski, W. S. Glaunsinger, and A. Navrotsky, J. Phys. Chem. Solids **39**, 941 (1978).

[37] P. D. Dernier and M. Marezio, Phys. Rev. B **2**, 3771 (1970).

[38] D. B. McWhan and J. P. Remeika, Phys. Rev. B **2**, 3734 (1970).

[39] M. W. Chase, *NIST-JANAF Thermochemical Tables*, 4th ed. (American Institute of Physics, Woodbury, NY, 1998).

[40] G. Henkelman, A. Arnaldsson, and H. Jónsson, Comput. Mater. Sci. **36**, 354 (2006).

[41] M. Imada, A. Fujimori, and Y. Tokura, Rev. Mod. Phys. **70**, 1039 (1998).

[42] J. Frenkel, Phys. Rev. **54**, 647 (1938).

[43] Y. Cui, B. Liu, L. Chen, H. Lup, and Y. Gao, AIP Adv. **6**, 105301 (2016).

[44] L. Chen, Y. Cui, S. Shi, B. Liu, H. Luo, and Y. Gao, RSC Adv. **6**, 86872 (2016).